Earth and Planetary Science Letters 505 (2019) 118–130

Contents lists available at ScienceDirect

Earth and Planetary Science Letters

www.elsevier.com/locate/epsl

Holocene uplift and rapid fluvial erosion of Iceland: A record of post-glacial landscape evolution

Gaia Stucky de Quay *, Gareth G. Roberts *, Dylan H. Rood, Victoria M. Fernandes

Department of Earth Science and Engineering, Imperial College London, South Kensington Campus, London SW7 2AZ, UK

ARTICLE INFO

Article history:
Received 31 May 2018
Received in revised form 12 October 2018
Accepted 16 October 2018
Available online 26 October 2018
Editor: M. Bickle

Keywords:
uplift
fluvial erosion
Iceland
Holocene
cosmogenic ^{3}He
landscape evolution

ABSTRACT

In actively deforming regions fluvial systems are strongly regulated by uplift. River geometries record histories of vertical motions that can be used to examine the driving forces generating topographic relief. Iceland's rapidly evolving landscapes provide an opportunity to disentangle histories of uplift generated by postglacial rebound, volcanism, dynamic support, and plate spreading. Broad knickzones observed along Iceland's large rivers, and its powerful waterfalls and deep canyons, hint that regional processes have generated significant relief. We combine high-resolution drone photogrammetry and cosmogenic ^{3}He dating of fluvial terraces to measure the erosional history of one of Iceland's largest knickzones, Jökulsárglúfur, in the northeast part of the island. Progressive younging of terraces indicates knickpoint propagation rates of up to ~70 cm a^{-1} during the last 8 ka. Knickpoint velocities appear to be controlled partly by toppling of basalt columns. These rates were used to calibrate a model that inverts Iceland's drainage networks for uplift rate histories. Calculated uplift and isostatic calculations indicate that rifting, sub-plate support, and isostatic adjustment resulted in tens to hundreds of meters of regional Holocene uplift. Our results suggest regional uplift and fluvial erosion can rapidly generate hundreds of meters of relief in post-glacial landscapes.

1. Introduction

Histories of topographic growth and decay contain information about evolution of tectonic and erosional processes at a range of scales. An important challenge is to develop observations and theory to constrain histories of landscape evolution. We examine Iceland, where topography and the geological record contain excellent evidence for regional and local uplift moderated by glacial and fluvial processes (Fig. 1; Geirsdóttir et al., 2007; Bjornsson, 2009). For example, stratigraphic records on- and offshore, crustal thickness, and basalt and ocean chemistry indicate a punctuated history of Neogene uplift and erosion of Iceland (Jones et al., 2002; Shorttle et al., 2010; Verhoeven et al., 2011; Parnell-Turner et al., 2014). Uplift measurements at spot locations from Global Positioning Satellite (GPS) and InSAR data have been used to constrain faulting, seismicity, magmatism, and post-glacial rebound (Sturkell et al., 2006; Pagli et al., 2007; Árnadóttir et al., 2009). Geomorphological and stratigraphic evidence for island-wide glaciation prior to 8 ka include hanging and U-shaped valleys, drop stones, moraines, drumlins, and striated bed rock (Spedding and Evans, 2002; Kjær et al., 2008). The last major deglaciation (Preboreal) in Iceland began at ~10 ka, when ice caps that previously extended to the modern coastline began retreating and reached their current extent at ~8 ka (Nordhdahl et al., 2008). Unloading of the lithosphere during deglaciation has generated up to ~100 m of uplift across large parts of the island, providing important constraints on mantle viscosity (e.g. Pagli et al., 2007).

Stratigraphy and historical accounts indicate that fluvial erosion in Iceland can generate several meters of relief in short amounts of time (hours to days) during high-discharge glacial outburst floods (i.e. jökulhlaups; Smith et al., 2000). Longitudinal river profiles extracted from ASTER GDEM and Landmælingar Íslands Hæðarlíkan (LMÍ) digital elevation data show that many of the island's large waterfalls (e.g. Dettifoss, Gullfoss, Goðafoss) sit within longer wavelength changes in slope (i.e. knickzones) that are tens to hundreds of kilometres wide and hundreds of meters high (Figs. 1b–e). The pervasiveness of knickzones throughout Iceland's drainage networks suggests that its erosional system is responding to regional changes in base level. Cross-sections through Icelandic topography show relief downstream of its large fluvial knickzones can exceed relief upstream (Fig. 2). These observations are consistent with field studies that indicate fluvial erosion can dramatically increase relief in previously glaciated landscapes (Koppes and Montgomery, 2009).

* Corresponding authors.
E-mail addresses: g.stucky-de-quay14@imperial.ac.uk (G. Stucky de Quay), gareth.roberts@imperial.ac.uk (G.G. Roberts).

https://doi.org/10.1016/j.epsl.2018.10.026

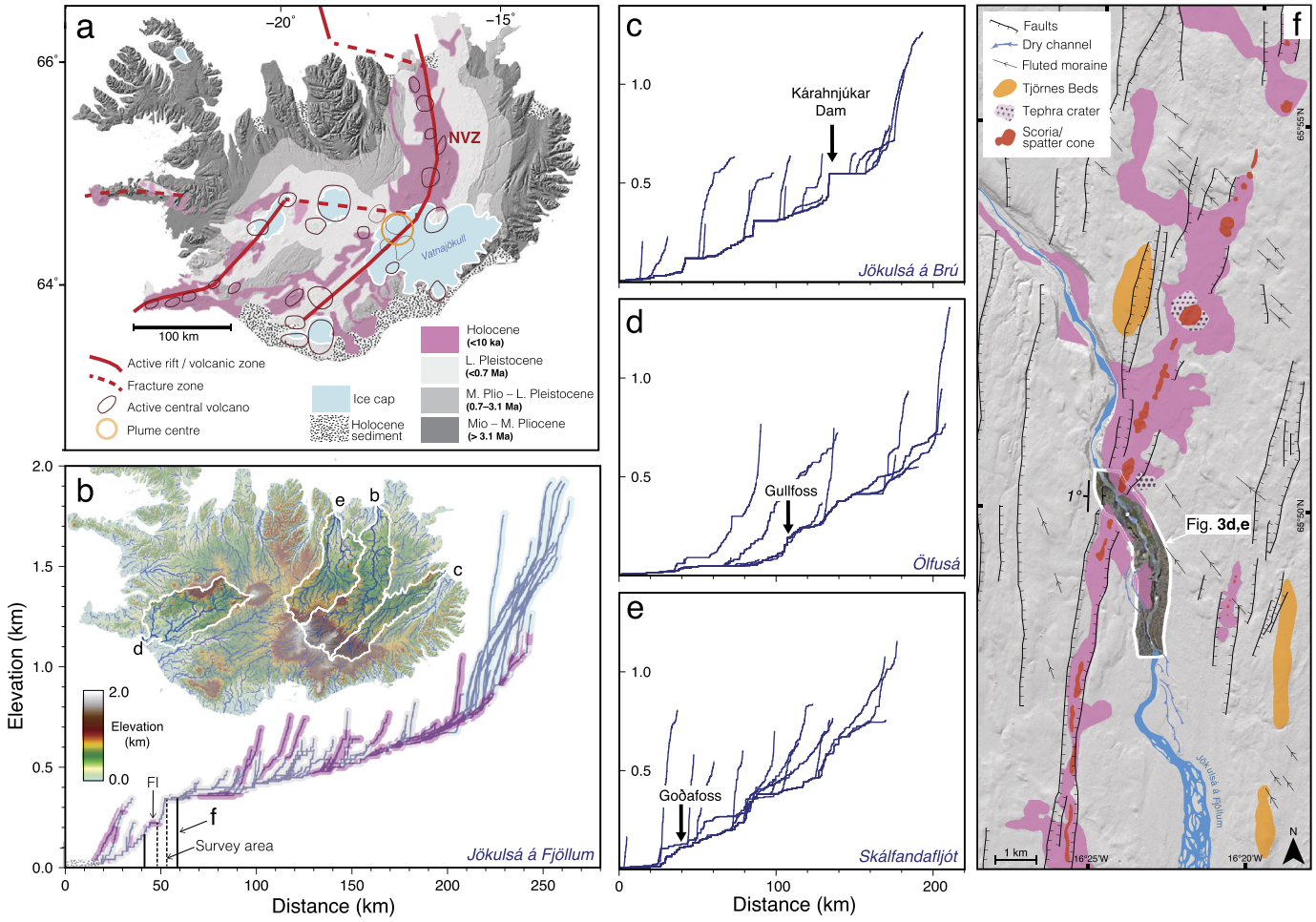

Fig. 1. (a) Map of Icelandic geology and topographic relief from ASTER GDEM (Jóhannesson and Sæmundsson, 1989; Tentler and Temperley, 2007; Martin et al., 2011). NVZ = Northern Volcanic Zone. (b) Longitudinal river profile extracted from LMÍ DEM and underlying geology of Jökulsá á Fjöllum. Note extent of survey area, see panel (f); Fl = fissure. (c)–(e) Longitudinal river profiles of Jökulsá a Brú, Ölfusá, and Skálfandafljót extracted from ASTER GDEM (see inset map in panel b). Y-axis = elevation (km). Black arrows = waterfalls and dams. (f) Jökulsárgljúfur canyon geology and ArcticDEM topography. White polygon = location of UAV DEM (see Fig. 3). (For interpretation of the colours in the figures, the reader is referred to the web version of this article.)

To determine the history of Iceland's post-glacial topography we measured erosion rates of the largest knickzone in Jökulsá á Fjöllum, which contains three large waterfalls (knickpoints): Selfoss, Dettifoss, Hafragilsfoss (Figs. 3a–c). Jökulsá á Fjöllum flows ∼200 km from its source beneath the Vatnajökull glacier to the sandur plains in Öxarfjörður in the Arctic Ocean and runs subparallel to the Northern Volcanic Zone, through the Jökulsárgljúfur canyon (Figs. 1a, 1b, & 1f). Total drainage area of the river is ∼8000 km^2 and maximum annual discharge is ∼500 m^3 s^{-1} (Baynes et al., 2015a). The mouth of Jökulsárgljúfur is located ∼45 km upstream from the coast and sits within the broad knickzone shown in Fig. 1b. The canyon has walls in excess of 100 m high, containing layered basalt flows with thicknesses between 5–50 m (Fig. 3d). The flows are composed of vertical and subvertical basalt columns. Three prominent fluvial terraces cut across lava flows and abut the Selfoss, Dettifoss, and Hafragilsfoss waterfalls (Figs. 3d & 3e). These observations suggest that terraces were abandoned due to waterfall retreat (e.g. Baynes et al., 2015a). The presence of flutes, scours, tool marks, potholes, and polished surfaces on the terraces show that fluvial abrasion plays an important role in generating relief from vertical incision (see Figs. 4a–d).

We combine field mapping and Unmanned Aerial Vehicle (UAV) imagery with cosmogenic ^{3}He dating of abandoned river terraces to constrain the canyon's erosional history. We compare our waterfall retreat rates to models of block toppling which make use of measured discharge along Jökulsá á Fjöllum. We use these data to calibrate models of spatio-temporal uplift across Iceland, which can then be compared to independent constraints of uplift, and can be used to assess the importance of fluvial, glacial, and tectonic processes in generating Iceland's modern topography.

2. Data & methods

2.1. UAV photogrammetry

A digital elevation model of the Jökulsárgljúfur canyon was generated using a DJI Phantom 4 drone and the Pix4Dmapper software (see Figs. 3d & 3e). The canyon was mapped as 12 separate flight missions with grids of surface area ∼400 × 400 m. Each grid contained 300–400 overlapping photographs. Camera angle was set to 60° to map canyon walls. Flight elevation was ∼90 m above land and water surfaces, which avoided most waterfall spray. Photographs from each mission were processed using Pix4Dmapper software to produce a high density 3D point cloud, which was used to generate the orthomosaic and elevation model. Ground control points were acquired using three 50 cm square targets for each grid using a Trimble Geo 7x and a Zephyr external GNSS antenna. Elevation models for each grid were georeferenced and corrected for altitude using the ground control points. Absolute horizontal and vertical errors are 40 cm and 70 cm, respectively. Further processing was performed using ESRI ArcGIS to remove noise due to

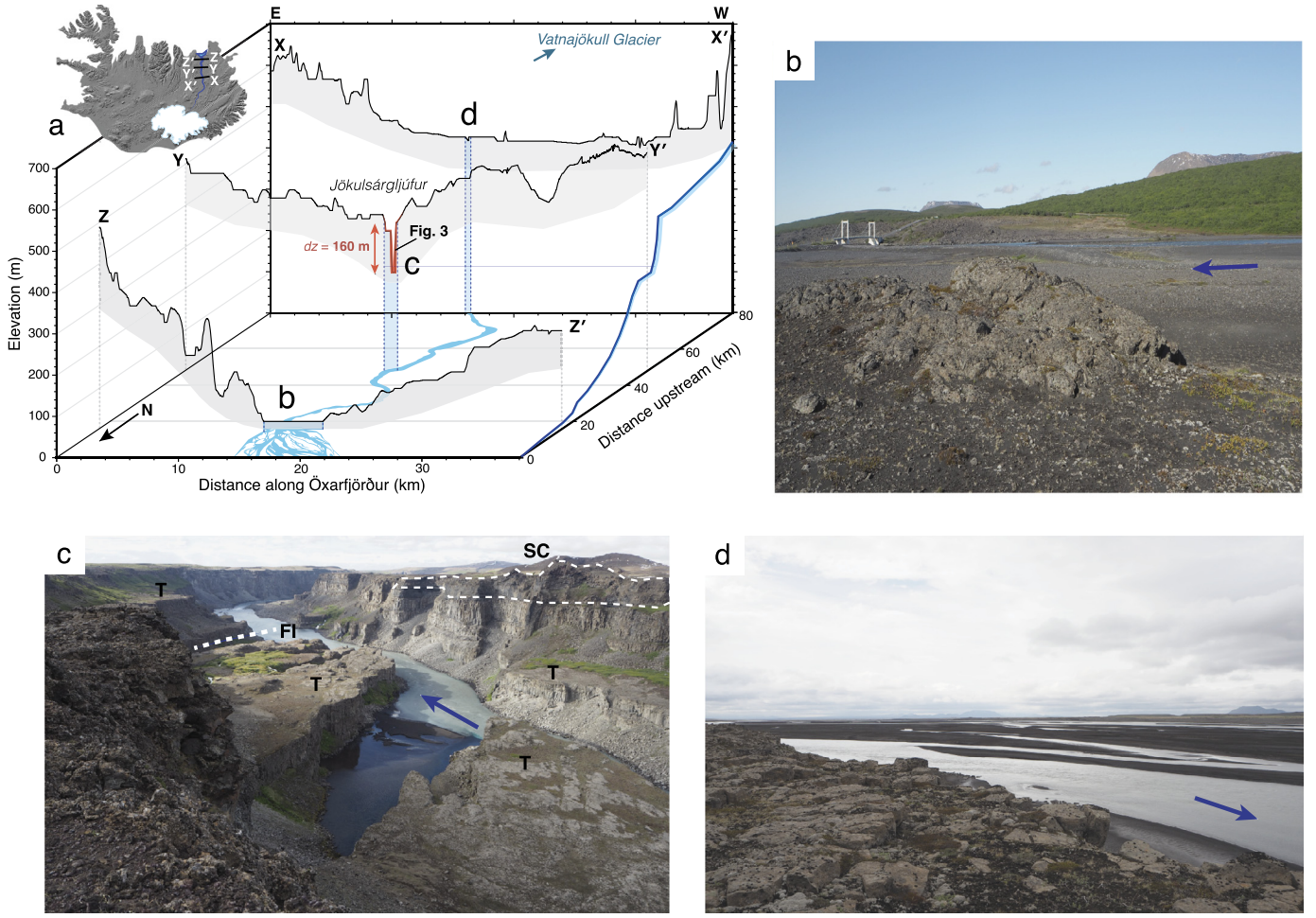

Fig. 2. (a) Cross-sections perpendicular to Jökulsá á Fjöllum extracted from LMÍ DEM; note inset map shows location of cross-sections. Light/dark blue curves = projected planform/longitudinal profiles of the river. Red = fluvial incision in Jökulsárgljúfur canyon (see Figs. 3 & 2c). Note broad U-shaped valley upstream. (b), (c), & (d) photographs of river at positions indicated in panel (a). White dotted lines = volcano-tectonic features: FI = fissure, SC = scoria cone and associated Holocene flow deposits; T = abandoned terraces.

waterfall spray, clouds, flowing water, and edge effects. The resultant digital elevation model has a horizontal and vertical resolution of up to 4 cm (Figs. 3d & 3e).

2.2. Cosmogenic ^{3}He dating

To determine exposure ages of abandoned terraces, samples were collected along Jökulsá á Fjöllum in June 2017 (Fig. 3e). ASTER, LMÍ, and ArcticDEM digital elevation data, satellite imagery, and field mapping were used to identify suitable sampling sites. Fluvial terraces were identified by their geometries (e.g. close to horizontal, abutting waterfalls; Fig. 3d) and presence of geomorphological markers such as scour marks, potholes, polishing, flutes, boring, striations (Figs. 4a–d). Twenty-five rock samples from three fluvial terraces were extracted for ^{3}He cosmogenic exposure dating. An additional sample was collected 40 km downstream at the mouth of the river, and one from a terrace in Jökulsá á Brú (see Table 1).

A cordless angle-grinder was used to extract ~5 × 2 × 2 cm rock cuboids from near-horizontal surfaces. A few samples were obtained from rock edges and extracted using a sledgehammer. We avoided sampling where there was evidence for soil and lichen. Crushing, sieving, magnetic, and density separation techniques were used to extract 150- to 250-µm-diameter olivine and pyroxene grains. Samples were purified by sonication in 2% (vol/vol) 2:1 HF:HNO_3 acid for 1 h at room temperature. Larger samples and those with adhering groundmass were also sonicated in 5% acid up to three times and dry-sieved at 150 µm. To remove mantle-derived ^{3}He trapped in melt and fluid inclusions, the samples were ground in propanol. This method avoids ^{3}He adsorption from the atmosphere (Protin et al., 2016). Up to 300 µm of the purified samples were placed into aluminium foil balls and fed into a vacuum where noble gases were extracted at 1250 °C (Blard et al., 2015).

^{3}He concentrations of samples were measured using a MAP 215-50 noble gas mass spectrometer in the Noble Gas Laboratory at the California Institute for Technology. Repeat measurements were made for four samples: AE03-2, AW07-2, CW01-2, CW06-2, with good agreement in ^{3}He concentration within error for each sample (Table 1). Exposure ages were calculated as $t = n/P$, where n = number of measured ^{3}He atoms, and P is cosmogenic ^{3}He production rate. The production rate at each sample site was calculated using

$$P = P_{ref} \times S_{EL} \times S_z \times S_{topo} \times S_{snow}. \quad (1)$$

We use reference production rate, $P_{ref} = 124 \pm 4$ at g^{-1} a^{-1}, calibrated for Iceland by independent radiocarbon dating (Licciardi et al., 2006). Spatial scaling, S_{EL}, varies as a function of elevation and latitude and was estimated using the scaling factors given by Stone (2000) who used a modified version of Lal (1991)'s approach. Additional scaling factors S_z, S_{topo}, and S_{snow} depend on sample thickness, topographic shielding, and snow cover, respectively. We solve an expanded version of Equation (1):

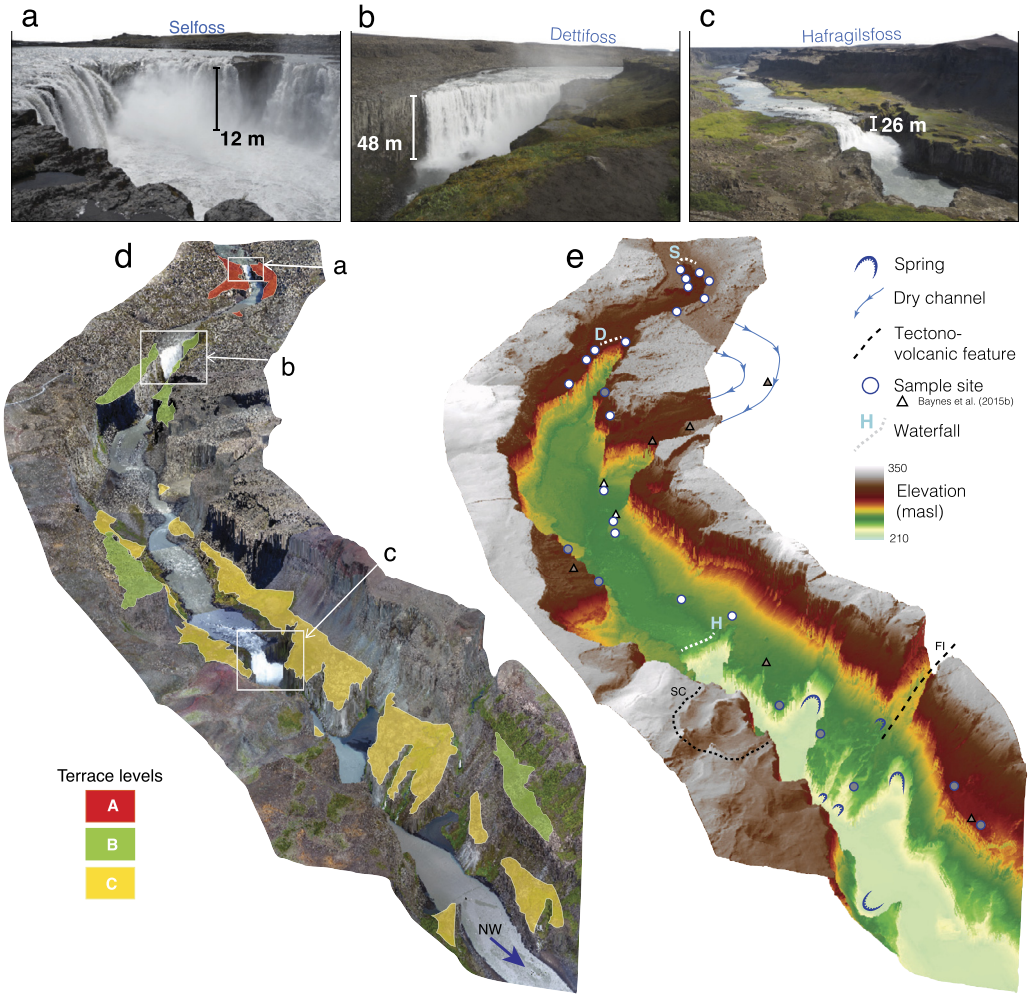

Fig. 3. (a)–(c) Photographs of the three largest waterfalls in the Jökulsárgljúfur canyon. Locations are shown in panel (d). (d) UAV DEM of the canyon draped by orthomosaic imagery (2× vertical exaggeration). Coloured surfaces = mapped terraces. DEM is 5 km long in field of view. Blue arrow indicates flow direction. (e) DEM of canyon with key geological/geomorphological observations and sample locations: S = Selfoss, D = Dettifoss, H = Hafragilsfoss, Fl = fissure, SC = scoria cone. White circles = samples collected in this study used to calculate retreat rates in Fig. 7; grey circles = samples not used to calculate retreat rates; white/grey triangles = samples from Baynes et al. (2015b).

$$P = P_{ref} \times \left[a + b\exp\left(-\frac{p}{150}\right) + cp + dp^2 + ep^3\right] \times \frac{\Lambda}{\rho z}\left[1 - \exp\left(-\frac{z\rho}{\Lambda}\right)\right] \times \left[1 - \frac{1}{2\pi}\sum_{i=1}^{n}\Delta\phi_i \sin^{3.3}\theta_i\right] \times \frac{1}{12}\sum_{j=1}^{12}\exp\left(-\frac{z_{s_j}\rho_s}{\Lambda}\right). \quad (2)$$

Spatial scaling S_{EL} is calculated using air pressure, p, which is a function of elevation, E, and can be calculated using $p = p_{sl}\exp\{[-gM/RL][\ln(T) - \ln(T - LE)]\}$, where p_{sl} = air pressure at sea-level (1013.25 × 10^2 Pa), g = gravitation acceleration (9.81 $\mathrm{m\,s^{-2}}$), M = molar weight of air (28.97 $\mathrm{g\,mol^{-1}}$), R = gas constant (8.314 $\mathrm{J\,mol^{-1}\,K^{-1}}$), L = adiabatic lapse rate (0.0065 K $\mathrm{m^{-1}}$) and T = air temperature at sea-level (288.15 K). Scaling coefficients $a = 71.8733$, $b = 863.1927$, $c = -0.207069$, $d = 2.0127 \times 10^{-4}$, $e = -6.6043 \times 10^{-8}$, which are appropriate for latitudes >60° (Stone, 2000). S_z calculates attenuation of cosmic rays in rock as a function of attenuation wavelength, Λ, density, ρ, and sample thickness, z. We set $\Lambda = 150$ $\mathrm{g\,cm^{-1}}$ and $\rho = 2.8$ $\mathrm{g\,cm^{-3}}$ (Gosse and Phillips, 2001; Marrero et al., 2016). Topographic shielding, S_{topo}, was estimated using a sighting clinometer to measure azimuth, ϕ_i, and inclination, θ_i, of n topographic obstructions along the horizon in a 2π arc from each sample site (Dunne et al., 1999). Finally, shielding due to snow cover, S_{snow}, was calculated. Maximum annual cumulative precipitation in Akureyri and Ásbyrgi is 400–500 mm of which ~50% falls as snow in 8 months each year (Eythorsson et al., 1971; Björnsson, 1980; Einarsson, 1984; Ólafsson et al., 2007; Crochet et al., 2007; Jónsdóttir and Uvo, 2009). We tested snow densities, ρ_s, and thicknesses, z_s, between $0.1 \le \rho_s \le 0.3$ g $\mathrm{cm^{-3}}$ and $0 \le z_s \le 25$ cm (Gosse and Phillips, 2001). Using a central value of $\rho_s = 0.2$ g $\mathrm{cm^{-3}}$ and $z_s = 12.5$ cm results in a snow shielding factor $S_{snow} = 0.989$ for all samples. All other values for scaling factors are sample-specific and are listed in Table 1. Olivine and pyroxene have similar ^{3}He production rates and variations in olivine:pyroxene do not add any significant age errors (Fenton et al., 2009).

A systematic sweep of parameters in the production rate model in Equation (2) was performed to estimate their contribution to uncertainties in calculated exposure ages (Fig. 5). Uncertainties in reference production rates and snow cover contributed the largest systematic error to calculated exposure ages (3.4% and 2.2%, respectively; Figs. 5a & 5d). Uncertainties in spatial scaling, sample thickness, and topographic shielding contribute errors < 0.5%. The

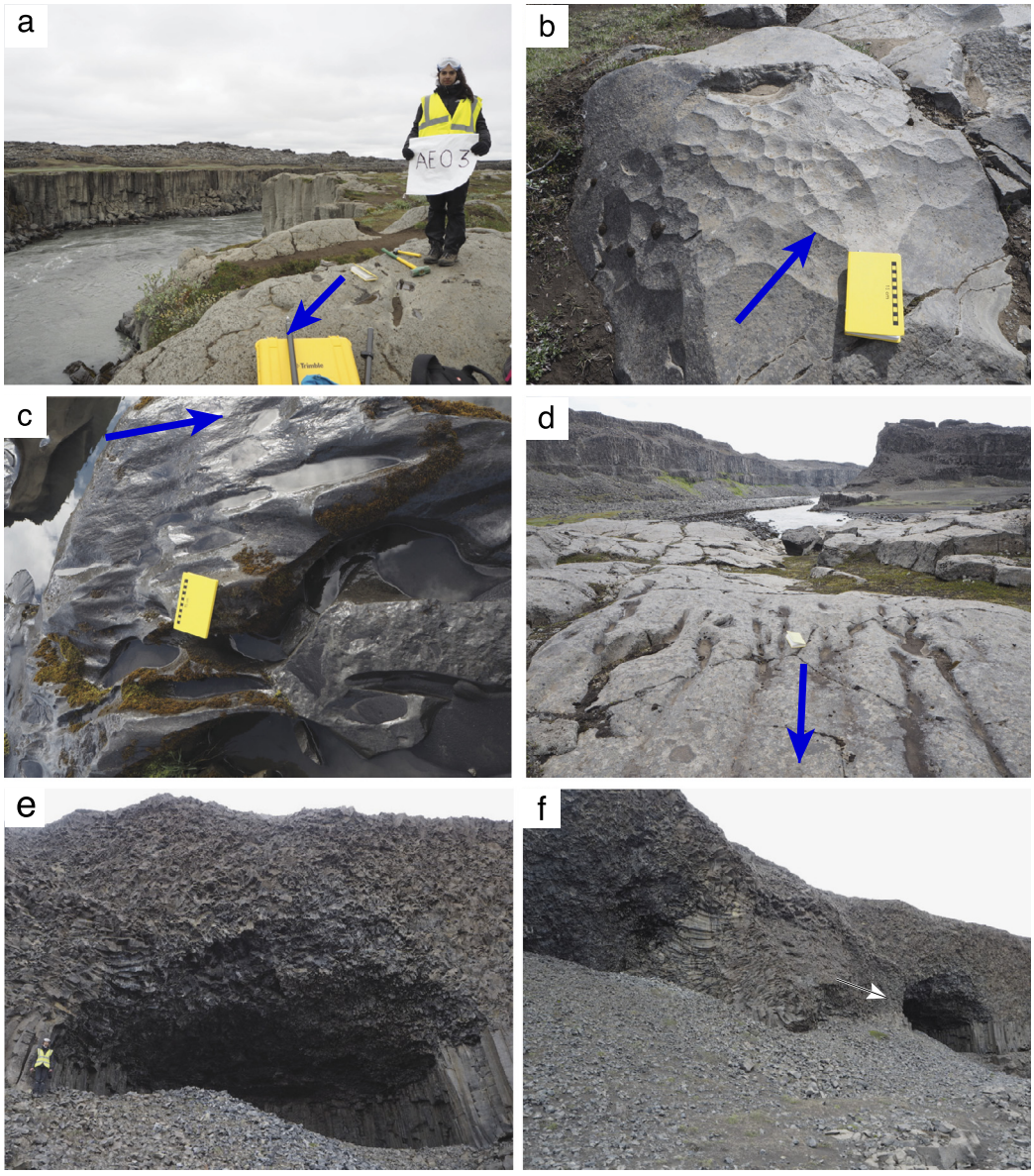

Fig. 4. Examples of fluvial erosion and sample sites along Jökulsárglúfur canyon terraces. (a) Example of sample site AE03. Note flute marks on terrace. Dark blue arrow = direction of river flow. (b) High density of scour marks on eastern side of Terrace B. (c) Flutes, potholes, and scour marks on Terrace B close to Dettifoss. (d) Tool marks and flutes at higher state of degradation on Terrace C. (e) & (f) Location of shielded sample used for correction of cosmogenic ^{3}He in Jökulsárglúfur. Top of cave is ~20 m from top of canyon. White arrow = location of cave on Terrace B (eastern side).

Lifton-Sato scaling schemes were used to test a range of time-dependent cosmogenic production scenarios, which incorporated temporal and spatial variability of geomagnetic and solar modulation of cosmic ray fluxes (Lifton et al., 2005; Sato and Niita, 2006). Sample data were propagated through the CRONUS exposure age calculator (Marrero et al., 2016). Results yielded an average difference in production scales of 1.8% compared to models that assume constant flux. We also tested the Dunai (2000) time-dependent scaling scheme used by Baynes et al. (2015b), which yielded an average difference of 2.2%. Samples BE05 and BW02, located close to the crest of Dettifoss, have exposure ages of 0 ka within error, which suggests that vertical erosion rates were sufficiently high that negligible ^{3}He accumulated prior to formation of the terrace (Terrace B).

A sample shielded from cosmic rays was collected from a cave in the canyon to correct for non-cosmogenic ^{3}He (Figs. 4e & 4f). The sample was collected from the back wall of the cave (>10 m from entrance) and close to its ceiling (>20 m from lava flow top) where incidence of cosmic rays is probably negligible. The sample acquired from this cave was assumed to be representative for the three terraces. The correction for non-cosmogenic ^{3}He is

$$n = n_t - n_s, \tag{3}$$

where n is the number of cosmogenic ^{3}He atoms in each sample, n_t is the total uncorrected number of ^{3}He atoms measured, and n_s is the number of ^{3}He atoms measured from the shielded (i.e. cave) sample, where $n_s = 38 \pm 23 \times 10^3$ at g^{-1}. Non-cosmogenic ^{3}He accounts for 3–73% of total ^{3}He measured in samples (mean = 14%; largest uncertainties are for the youngest samples, e.g. BE05). Errors in exposure age, δt, were calculated by propagating errors in measured ^{3}He atoms, $\delta n = \sqrt{\delta n_t^2 + \delta n_s^2}$, and production rate, $\delta P = P_{ref} S \sqrt{(\delta P_{ref}/P_{ref})^2 + (\delta S_{snow}/S_{snow})^2}$, where $S = S_{EL} \times S_z \times S_{topo} \times S_{snow}$, using

Table 1
Sample data used to measure cosmogenic ^{3}He exposure ages of fluvial terraces in northeast Iceland.

Sample name[a]	Latitude (°)	Longitude (°)	Elevation (m)	Distance from knickpoint (m)[b]	Thickness (cm)	Thickness scaling factor, S_z	Topographic shielding factor, S_{topo}	Lal & Stone scaling factor, S_{EL}	Production rate (at g^{-1} yr^{-1}) $\pm1\sigma$	Olivine + pyroxene mass (g)	Cosmogenic ^{3}He ($\times10^3$ at g^{-1}) $\pm1\sigma$[c]	Exposure age (yr) $\pm1\sigma$
This work:												
AW01	65.80614	−16.38841	316.5	176	2	0.982	1.000	1.389	167 ± 6	0.307	392 ± 40	2347 ± 257
AE02	65.80826	−16.38830	317.7	392	2	0.982	1.000	1.391	167 ± 6	0.287	526 ± 41	3143 ± 273
AE03	65.80700	−16.38749	317.2	255	14	0.880	1.000	1.390	150 ± 6	0.318	582 ± 45	3880 ± 332
AE03-2										0.439	635 ± 37	4232 ± 295
AE04	65.80593	−16.38647	316.8	125	2	0.982	1.000	1.390	167 ± 6	0.342	446 ± 37	2666 ± 245
AW05	65.80716	−16.38978	316.9	252	9	0.921	1.000	1.390	157 ± 6	0.318	673 ± 43	4291 ± 319
AW06	65.80954	−16.39037	318.2	577	2	0.982	0.999	1.392	167 ± 6	0.347	1028 ± 45	6141 ± 355
AW07	65.81160	−16.38877	321.2	820	2.5	0.977	1.000	1.396	167 ± 6	0.318	1240 ± 59	7418 ± 450
AW07-2										0.263	969 ± 54	5799 ± 386
BE01	65.81844	−16.38345	299.7	397	2	0.982	0.998	1.367	164 ± 6	0.095	216 ± 85	1316 ± 519
BW02	65.81406	−16.38551	300.4	40	2	0.982	0.994	1.368	164 ± 6	0.025	43 ± 302	262 ± 1842
BW03	65.81910	−16.38670	303.7	–	2	0.982	0.993	1.372	164 ± 6	0.383	456 ± 38	2777 ± 252
BE04	65.81608	−16.38339	301.7	133	2.5	0.977	0.988	1.370	162 ± 6	0.276	157 ± 38	965 ± 239
BE05	65.81494	−16.38339	298.2	8	2	0.982	0.995	1.365	163 ± 6	0.101	14 ± 78	87 ± 475
BW06	65.82083	−16.38814	298.6	825	3	0.973	0.957	1.365	156 ± 6	0.037	232 ± 207	1488 ± 1329
BW07	65.83801	−16.41459	284.9	–	2.5	0.977	0.998	1.347	161 ± 6	0.062	1387 ± 144	8611 ± 955
BW08	65.83904	−16.41588	279.3	–	2.5	0.977	0.998	1.340	160 ± 6	0.042	364 ± 182	2270 ± 1141
BE09	65.83015	−16.39092	308.3	–	11	0.904	0.998	1.378	152 ± 6	0.300	1931 ± 65	12664 ± 636
BE10	65.83171	−16.39376	309.0	–	8	0.929	0.998	1.379	157 ± 6	0.317	1698 ± 67	10825 ± 587
CW01	65.82427	−16.38953	247.7	1215	2	0.982	0.989	1.299	155 ± 6	0.310	329 ±41	2127 ± 277
CW01-2										0.486	313 ± 31	2027 ± 214
CW02	65.82623	−16.39138	247.6	1461	2.5	0.977	0.971	1.299	151 ± 6	0.204	314 ± 48	2079 ± 326
CW03	65.82692	−16.39184	247.5	1537	2	0.982	0.982	1.299	154 ± 6	0.406	397 ± 40	2585 ± 278
CW04	65.83094	−16.40128	246.8	2123	2.5	0.977	0.968	1.298	151 ± 6	0.320	466 ± 42	3092 ± 718
CW05	65.83022	−16.39786	244.2	1996	2	0.982	0.983	1.294	153 ± 6	0.098	302 ± 90	1974 ± 593
CW06	65.83446	−16.40524	238.3	–	5	0.955	0.991	1.287	149 ± 6	0.330	367 ± 45	2455 ± 314
CW06-2										0.480	211 ± 31	1410 ± 214
CW07	65.83537	−16.40770	236.3	–	13	0.888	0.984	1.284	138 ± 5	0.394	214 ± 38	1553 ± 280
CW08	65.83707	−16.40978	231.4	–	2.5	0.977	0.985	1.278	151 ± 6	0.300	233 ± 38	1545 ±258
JF01[d]	66.03254	−16.44017	44.0	–	4	0.963	1.000	1.052	124 ± 6	0.090	61 ± 87	494 ± 698
JB03[e]	65.10672	−15.53180	353.0	–	12.5	0.892	1.000	1.439	157 ± 6	0.034	92 ± 222	584 ± 1413
Sh-B[f]	65.82083	−16.38840	–	–	–	–	–	–	–	0.337	–	–
Baynes et al. (2015b)[g]:												
DW2	65.81813	−16.39859	320.0	–	≤5				166	0.915	355 ± 126	2150 ± 750
DW3	65.82256	−16.39517	324.0	–	≤5				167	0.807	1005 ± 195	6000 ± 1200
DW4	65.82247	−16.39180	298.0	–	≤5				163	0.613	230 ± 170	1450 ± 1050
DW5	65.82389	16.38962	253.0	1080	≤5				156	0.906	235 ± 128	1500 ± 800
DW6	65.82634	−16.39141	255.0	1275	≤5				156	1.171	281 ± 161	1800 ± 1000
DW7	65.83358	16.40515	244.0	–	≤5				155	0.808	244 ± 121	1600 ± 800
DE1	65.83107	−16.39155	309.0	–	≤5				164	0.891	1149 ± 389	7500 ± 2800
AR1	65.99732	−16.51454	131.0	–	≤5				139	0.723	1286 ± 276	9850 ± 2650

[a] First letter = Terrace A/B/C; second letter = East/West side of canyon; appended "−2" indicates repeat sample measured for ^{3}He concentrations.
[b] Distance to knickpoints calculated by extracting downstream distance along lines parallel to river flow on either side of river. Samples without distances are not included in retreat rate calculations as they are not though to represent past location of waterfall (e.g. wrong topographic level; BW03).
[c] Cosmogenic ^{3}He concentrations corrected for machine background and non-cosmogenic ^{3}He, with uncertainties propagated in quadrature.
[d] Sample collected from mouth of Jökulsá á Fjöllum.
[e] Sample collected from Jökulsá á Brú.
[f] Shielded sample collected from cave in Terrace B (Data & Methods; Figs. 4e & 4f).
[g] Samples collected by Baynes et al. (2015b). Values shown for ^{3}He concentrations and exposure ages were determined by taking maximum range of possible values and assigning an average ± total error. Note that production rates were calculated using the Dunai (2000) time-variant scaling scheme. Re-calculating our sample production rates using the Dunai (2000) scale gives an average error of 2.2%, indicating choice of scaling scheme has limited effect on exposure ages. Sample DW8 is not included as it contains only an upper limit. Note AR1 collected from Ásbyrgi close to river mouth.

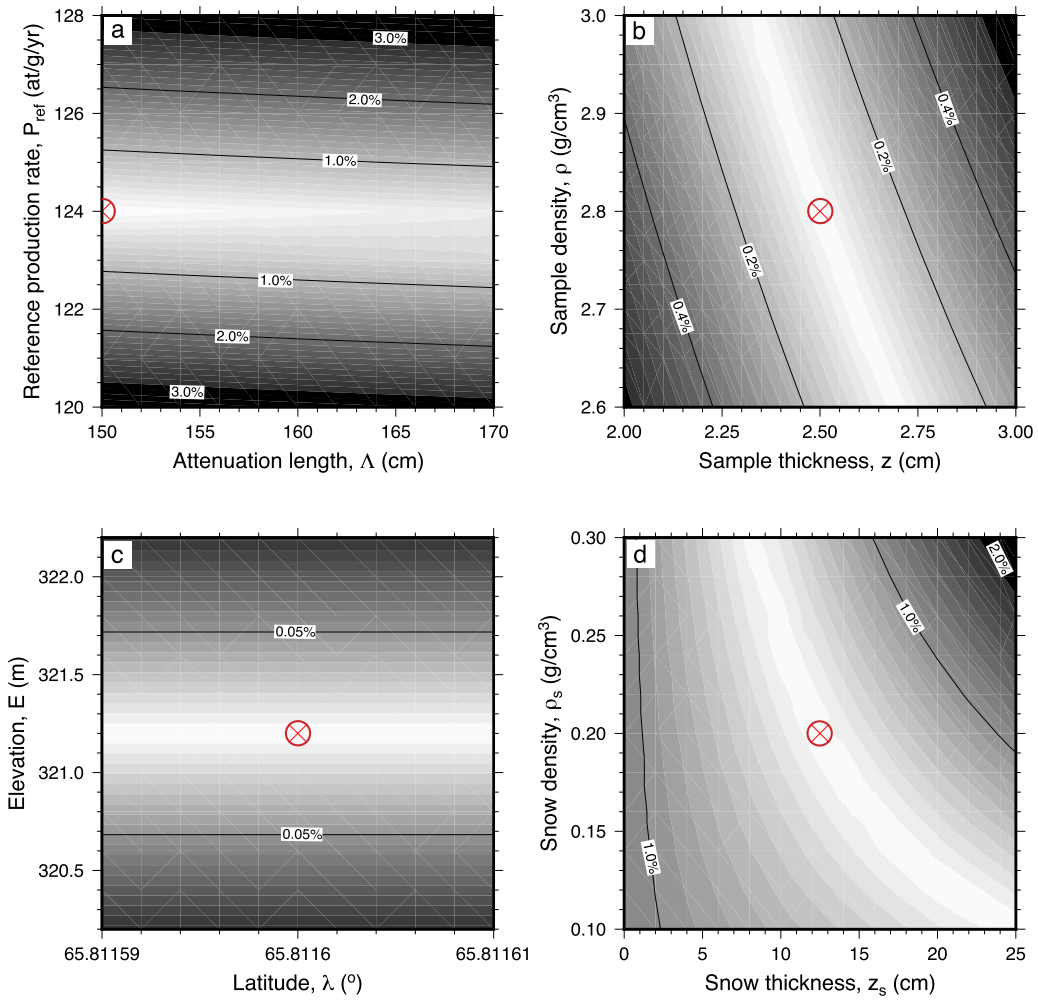

Fig. 5. Exposure age differences from co-variations of cosmogenic ^{3}He dating parameters for sample AW07. Colour scale equals percent difference between central value (red cross-hairs) and models run with parameter values shown by the axes. (a) Relative change in exposure age for varying production rate and attenuation length. Note >3% error for P_{ref}. (b) Relative change in exposure age for sample thickness and density. (c) Relative change in exposure age due to spatial scaling factors, elevation and latitude. Note 65.81160 ± 0.00001° corresponds to ∼±1 m error. (d) Relative change in exposure age for snow thickness and snow density.

$$\delta t = |t| \times \sqrt{\left(\frac{\delta n}{n}\right)^2 + \left(\frac{\delta P}{P}\right)^2}, \tag{4}$$

which assumes that uncertainties in spatial scaling, sample thickness, and topographic shielding are negligible. Samples with masses < 0.05 g and those with small measured ^{3}He concentrations (< 10^5 at g^{-1}) result in larger uncertainties due to difficulty in detecting very low ^{3}He concentrations (e.g. samples BE05, BW02, JB03, JF01; Table 1). The low ^{3}He concentrations in these samples is close to the detection limit for ^{3}He (< 50 ×10^3 at g^{-1}; Gosse and Phillips, 2001). This results in 1σ errors which are larger than the age of the sample for ages $\lesssim$ 500 yr (e.g. 87 ± 475 a, sample BE05 in Table 1).

The stratigraphy of columnar basalts in the canyon indicates that the terraces are located ∼4, 15, and 7 m below the top of lava flows. This mapping was performed by measuring the vertical distance between vesicular, ropey lava flow tops to the extrapolated height of the eroded terraces. These depths are much larger than the cosmic ray attenuation depth (∼1.5 m), which suggests that they would not have accumulated significant amounts of ^{3}He before their exposure as fluvial terraces (i.e. no inheritance).

3. Exposure ages and retreat rates

We combine the ^{3}He exposure ages with measurements of distance between samples and waterfalls from our UAV digital elevation model (Fig. 6). Calculated exposure ages vary between 0 years and 8 ka and young towards waterfalls. Linear regression of the data yields average knickpoint retreat velocities (see Fig. 7). Samples collected from terraces abutting Selfoss have exposure ages of 2–8 ka and yield a retreat rate of 10.6 ± 1.0 cm a^{-1}. Samples from terraces abutting Dettifoss indicate a retreat rate of 68.7 ± 0.1 cm a^{-1}. We note that linear regression of these datasets has R^2 values of 0.94 and 0.92, respectively. Retreat rates calculated for terraces at the top and bottom of the Dettifoss are consistent and exposure ages converge at the modern waterfall (Fig. 7c). Uncertainties in reference production rates and snow cover contributed the largest systematic error in calculated exposure ages. We assumed that errors are uncorrelated and propagated uncertainties in reference production rates, snow cover, and measured ^{3}He to generate the error bars shown in Fig. 7. Importantly, uncertainties in reference production rates and snow cover affect absolute ages of terraces but do not change their relative ages which are used to calculate knickpoint retreat rates.

Not all samples collected were used to measure retreat rates (see grey vs. white circles in Figs. 3e & 6c). Samples collected downstream of Hafragilsfoss (CW06, CW06-2, CW07, CW08) were

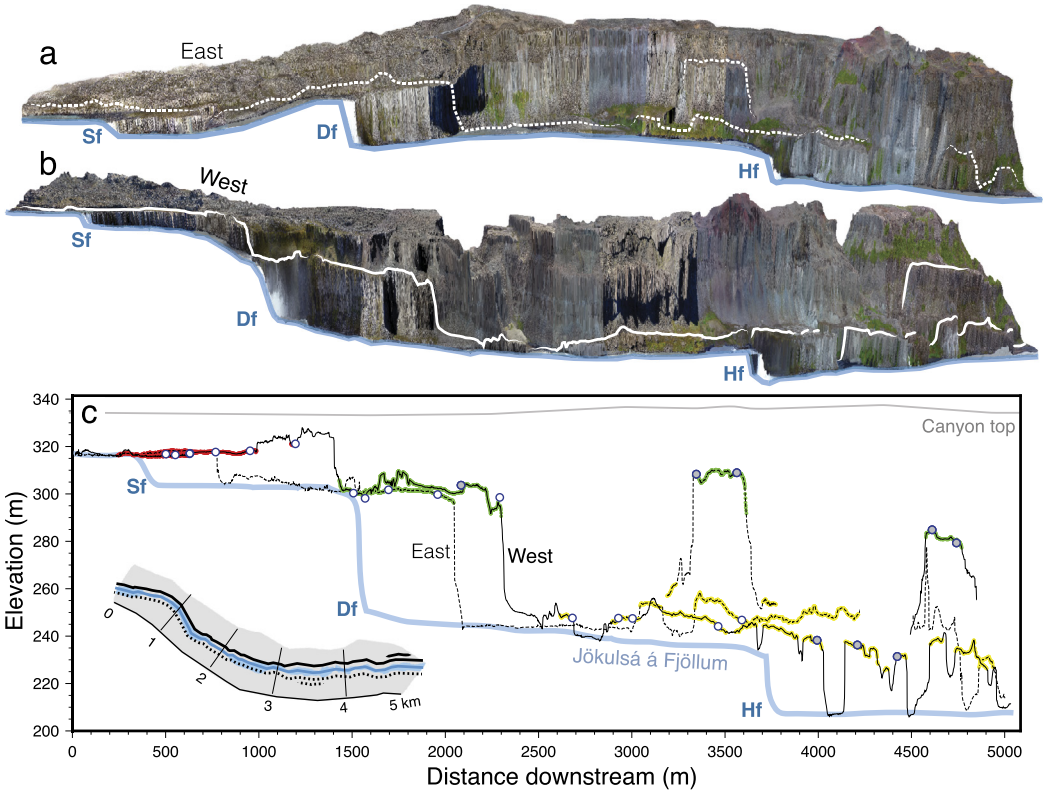

Fig. 6. Fluvial terraces in Jökulsárgljúfur canyon. (a–b) UAV orthomosaic image (5× vertical exaggeration) of eastern and western side of canyon. Blue line = modern river. Sf = Selfoss, Df = Dettifoss, Hf = Hafragilsfoss. Dashed/solid white line = fluvial terraces on eastern/western sides of the canyon. (c) Solid/dashed black lines = trace of fluvial terraces on western/eastern side of Jökulsárgljúfur (see inset map for location). Red/green/yellow = mapped and sampled terraces (see Fig. 3d). Grey-filled circles = locations of samples used to calculate retreat rates. Empty circles = additional samples collected (see Table 1). Blue = longitudinal river profile.

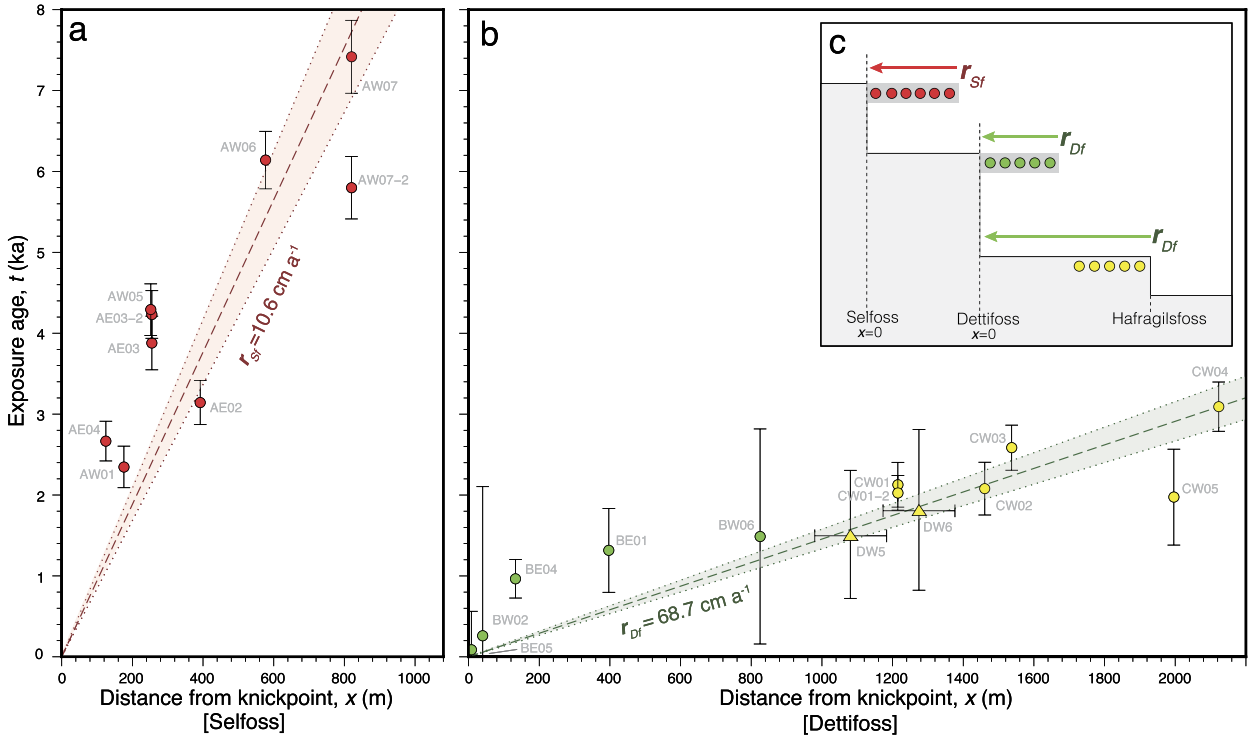

Fig. 7. (a) & (b) Exposure age of samples as a function of distance from the Selfoss and Dettifoss waterfalls. Errors are propagated from measurements of ^{3}He atoms and estimated cosmogenic production rates. Circles = samples collected in this study; triangles = samples from Baynes et al. (2015b). Colours correspond to terrace levels in Fig. 3d. Labelled dashed/dotted lines = best-fitting regression lines/$\pm 1\sigma$ of the means. r_{Sf}/r_{Df} = retreat rate of Selfoss/Dettifoss; R^2 = 0.94 and 0.92 for Selfoss and Dettifoss samples, respectively. Distance of samples from knickpoints was measured by taking location of samples along either east- or western dotted transects shown in inset of Fig. 6c; distance errors are less than a few meters. Note we estimate distance uncertainties for the samples acquired by Baynes et al. (2015b) using our map of the canyon. (c) Schematic of sample locations and retreat rates for Selfoss and Dettifoss.

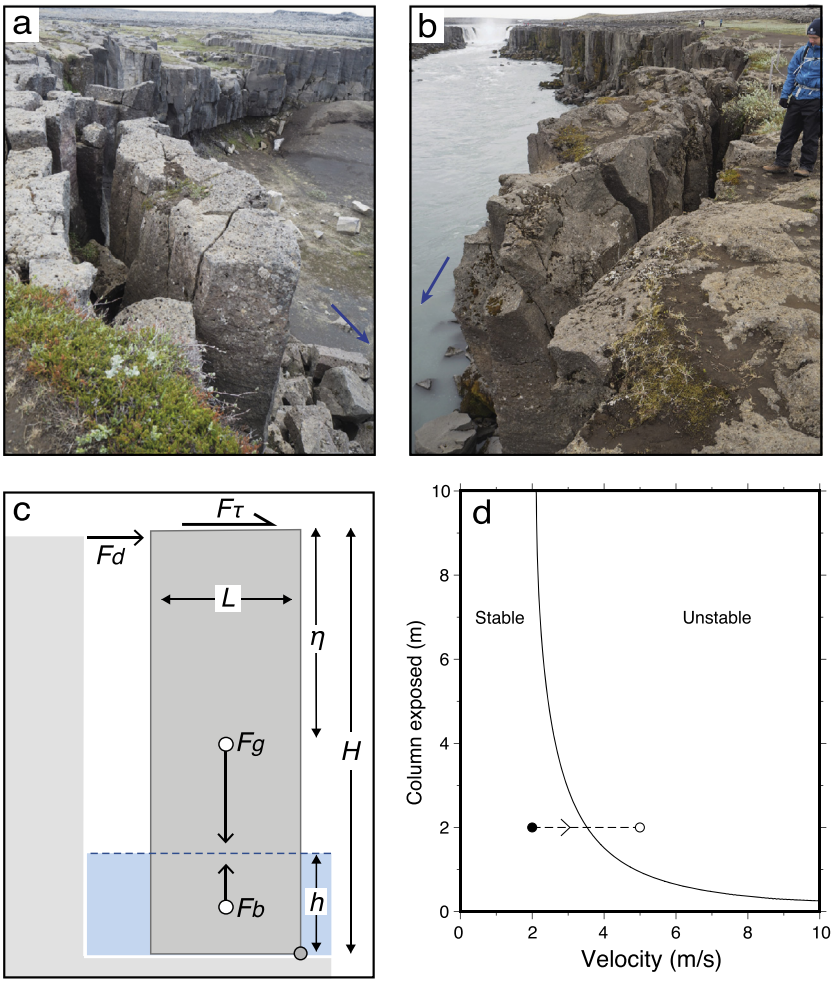

Fig. 8. (a) & (b) Examples of detached and toppled blocks on eastern & western sides of Terrace A, respectively. Note Selfoss in the background. (c) Schematic showing the forces on a rectangular rock column (e.g. Lamb and Dietrich, 2009, see text for details). Grey circle = pivot point for moment calculations. (d) Stability of a column of rock as a function of flow velocity and the amount of column (length) exposed to the flow calculated using Equation (9). Black/white circles = transition from stable block to unstable block for increased flow velocities (see body text for details).

not considered since they may have been affected by recent fissuring and lava emplacement during the Holocene. Samples collected on discontinuous terraces (BW03, BW07, BE08, BE09, BE10) were also not used. Lastly, due to their location outside of the knickzone and very young ages (~0 ka), samples JF01 (Jökulsá á Fjöllum mouth) and JB03 (Jökulsá á Brú) were not used to determine an incision rate but are included in Table 1.

4. Knickzone origin

How were Jökulsá á Fjöllum's knickzone and its waterfalls generated? The gradual decrease in ages of terraces towards waterfalls probably precludes formation in a single event, for example during catastrophic megafloods (cf. Waitt, 2009; Alho et al., 2005; Baynes et al., 2015b). Figs. 3d & 3e show that a large fissure cuts across the river downstream of Hafragilsfoss, generating a large valley, as well as associated springs, scoria cones, and dykes. The associated Rauðuborgir-Randhólar crater row and Sveinar graben are part of fissure systems linked to the volcanic centres in the Northern Volcanic Zone. The fissures contain crater rows distributed linearly in a roughly N–S orientation for ~30 km. Tephrochronological dating suggests the fissures erupted at ~ 8.5 ka, and may have temporarily dammed the river (Elíasson, 1974). Four observations suggest that it is unlikely these fissures generated the knickzone or waterfalls. First, the knickzone initiates downstream of the fissures (see FI in Fig. 1b). Secondly, change in elevation of the longitudinal river profile across the fissures is a few meters. Thirdly, there are waterfalls downstream of the fissures (e.g. Réttarfoss and Vígabjargsfoss). Finally, broad knickzones and large waterfalls (e.g. Goðafoss, Gulfoss) exist along all major Icelandic rivers.

Field and satellite mapping shows many of Iceland's rivers intersect fluted moraines, tephra layers, conglomerate beds, lava flows with a range of jointing and fracturing orientations, and fissure swarms which formed scoria, spatter cones, and dykes (Figs. 1f & 3d). Jökulsá a Fjöllum's substrate includes basalts that joint and fracture at a columnar (meter) scale, which indicates that substrate probably plays a role in setting erosion rates at short length scales (Baynes et al., 2015b, 2018). The collapse of columns generates relief of a few meters to a few tens of meters at wavelengths $\lesssim$ 10 m along the river.

5. Process of waterfall retreat

A few observations suggest that block toppling plays an important role in determining the retreat rate of waterfalls in the Jökulsárglúfur canyon. First, the edges of the waterfalls typically coincide with edges of vertically jointed columnar basalt. Secondly, in many places waterfall edges show evidence of tensional failure along the joints and collapsed columns litter the bottom of the canyon downstream of the waterfalls (Figs. 8a & 8b). To estimate the discharge required to detach these blocks we calculate rotational moments of an ideal column of basalt. These calculations

are combined with contemporary records of discharge to estimate waterfall retreat rates, which can be compared to our estimates of long-term knickpoint retreat. Our approach builds on Lamb and Dietrich (2009)'s torque calculations and Baynes et al. (2015b)'s synthesis of discharge measurements. Block stability is calculated as a function of the rock column mass, drag, shear, and buoyancy forces. We assume a very simple scenario in which friction at the base of the column is sufficiently high to inhibit sliding and the column is vertical and of unit width (Fig. 8c).

Drag is generated by water on the column of rock and its force, F_d, can be expressed as

$$F_d = \frac{1}{2}\rho_w C_d u^2 \eta, \tag{5}$$

where ρ_w is the density of water (1000 kg m^{-3}), C_d is the dimensionless drag coefficient, which is determined empirically and of O(1) (e.g. Batchelor, 1967). u is water velocity and η is the length over which the force is applied. The shear force generated by water at the top of the column can be calculated as

$$F_\tau = \tau_\circ L \approx \rho_w g h \frac{\mathrm{d}z}{\mathrm{d}x} L, \tag{6}$$

where g is gravitational acceleration (9.81 m s^{-2}), $\mathrm{d}z/\mathrm{d}x$ is channel bed slope, which we estimate to be O(10^{-3}), and L is the width of the column, which is O(1) m (see Figs. 8a & 8b; Supplementary Information in Baynes et al., 2015b). This estimation of shear force is wrong in detail as flow accelerates at the lip of column in response to reduced pressure downstream (i.e. as the water falls into air), but is probably of the correct order (Equations (6A)–(7) in Lamb and Dietrich, 2009). The buoyancy force generated as a result of water displaced by the column can be expressed as

$$F_b = \rho_w g L h, \tag{7}$$

where h is the depth of the water in which the column sits. The force generated by the mass of the ideal column of rock is

$$F_g = \rho_r g L H, \tag{8}$$

where ρ_r is the density of the rock column (∼2800 kg m^{-3}). By calculating the moments (torques) generated by these forces on the block we can estimate whether or not it will topple. Using Equations (5)–(8) and the lengths given in Fig. 8d indicates that the block will not topple if

$$\frac{\frac{1}{2}L\left(F_g - F_b\right)}{F_d(H - \eta/2) + F_\tau H} \geq 1. \tag{9}$$

Note that Equation (9) is slightly different to that given by Lamb and Dietrich (2009) and used by Baynes et al. (2015b) because we use the centroid of drag forces to calculate the rotational moment. In practice this modification makes a small difference to solutions to this equation in most circumstances. In some places within the canyon, rock columns are detached from the main wall by a few centimetres to ∼1 m, which suggests that we should consider the increase in velocity of water as it falls from the lip of the intact wall before hitting these blocks in our calculation of drag forces. Our simple approach to this problem assumes that the water remains as a jet as it falls and that its velocity $u = \sqrt{u_x^2 + (gx/u_x)^2}$, where u_x is the horizontal velocity of the water as it leaves the lip and x is the distance between the lip and the column of rock being impinged upon. For example if we assume $u_x = 2$ m s^{-1} and $x = 1$ m then $u = 5.3$ m s^{-1}. Note that we have not considered the angular impingement of flow on the column in our drag force calculations for simplicity. The history of discharge in the Jökulsárglúfur canyon is not well understood over the timescales of interest but there exists some modern constraints on flow velocities and discharges from the Grimsstadir gauging station ∼25 km upstream of Selfoss. Maximum discharge recorded between 1973–1979 at Grimsstadir was ∼470 m^3 s^{-1} and in 2001 average flow velocities were 2 m s^{-1} between the gauging station and Selfoss (Henriksen, 2005; Baynes et al., 2015b).

We estimate the stability ratio for a range of flow velocities, which can be related to discharge and flow depths (Equation (9)). For simplicity we approximate the cross-sectional area of the flow to either isosceles triangles or rectangles, which are broadly appropriate for the canyon. We assume flow velocity throughout the channel is constant. We can now estimate the stability of a column of rock as a function of flow velocity and the amount of column (length) exposed to the flow (Fig. 8d). For simplicity we assume the rock column is 1 m in length, 10 m high and that it is sitting in water 5 m deep (Fig. 8c). These simple calculations suggest that flow velocities of ≥ 3 m s^{-1} or more can topple a block that is exposed to more ≥ 2 m of the flow. Such flow velocities can be generated by a discharge of 500 m^3 s^{-1} and flow depths and widths of a few meters and a few tens of meters, respectively (cf. Henriksen, 2005). These observations suggest that maximum annual flow velocities in the canyon are large enough to make most exposed columns topple even without increasing velocities as water falls from the edge of the intact walls. Comparison with contemporary estimates of maximum annual discharge, flow depths and velocities suggest that these blocks should topple at a rate of approximately 1 per year to 1 per decade, which suggests a retreat rate of up to ∼0.1–1 m a^{-1}, which is broadly consistent with our estimated long term retreat rates of waterfalls in the canyon (up to 0.7 m a^{-1}). Importantly, lower waterfall heights require higher discharge to be unstable, which probably explains why Selfoss is retreating at a much lower velocity than Dettifoss (Fig. 7).

At a larger scale Jökulsá a Fjöllum's broad knickzone and fluvial terraces cross-cut different lithologies without significant changes in relief (Fig. 1b). No large tributaries join Jökulsá á Fjöllum in Jökulsárgljúfur. A dry channel west of the canyon has been interpreted as a manifestation of time-dependent discharge (Baynes et al., 2015b, Figs. 1f & 3d). In the northern section of the canyon groundwater springs merge with Jökulsá a Fjöllum's trunk river (Fig. 3e). These changes in discharge coincide with meter-scale changes in relief of the longitudinal river profile. These observations suggest that substrate and changes in discharge can generate ∼10 m of relief in Jökulsá á Fjöllum at wavelengths of a few meters to tens of meters. They cannot explain the shape of the river's broad knickzone, which has an amplitude of ∼500 m and wavelength of ∼100 km.

These observations suggest that the amplitude of Jökulsá á Fjöllum's knickzone is too large to have been generated solely by fissuring, lithological variations, or changes in discharge. The presence of broad knickzones along all of Iceland's large rivers indicate that inverting for a spatio-temporal history of uplift might yield useful insights into regional topographic support.

6. Calibration of Holocene erosional model

Using calculated erosion rates, we estimate the location of Jökulsá á Fjöllum's knickzone at the end of the Preboreal glaciation by assuming that uplift, $U = 0$, and solving a simplified version of stream power erosional model, such that

$$\frac{\partial z}{\partial t} = -v A(x)^m \frac{\partial z}{\partial x}, \tag{10}$$

where $\partial z/\partial t$ is the rate of change of elevation, A is upstream drainage area, x is distance from the mouth of the river, and v and m are positive erosional constants that must be calibrated (Rosenbloom and Anderson, 1994; Whipple and Tucker, 1999). If

we assume that $m = 0.5$, which is often used for fluvial systems, an appropriate value of v can be determined using knickzone retreat rates from Jökulsá á Fjöllum. Substituting $\mathrm{d}x/\mathrm{d}t = 68.7 \pm 0.1$ cm a^{-1}, $A = 6.79 \pm 0.4 \times 10^9$ m^2 into $\mathrm{d}x/\mathrm{d}t = vA(x)^m$ yields $v = 8.3 \pm 0.5$ Ma^{-1}. By solving, $L = \int_{\circ}^{T} vA(x)^m \mathrm{d}t$, we estimate the position of the knickpoint, L, at time, $T = 10$ ka. Since A is approximately constant for several km downstream of Dettifoss, a useful rule of thumb is, $L \approx T\mathrm{d}x/\mathrm{d}t$. We use the retreat rate derived from Dettifoss due to the waterfall's larger size compared to Selfoss ($\sim 4\times$). Solutions to these simple calculations suggest the knickpoint propagated to its current position from $\sim$7 km downstream, close to Hólmatungur where Réttarfoss and Vígabjargsfoss are located today (65.88° N, 16.88° W). We use the calibrated erosional model to invert our inventory of extracted rivers for a spatio-temporal uplift rate history.

7. River profile inversion

Drainage networks were extracted from the ASTER GDEM (resolution $\sim 26 \times 26$ m) and the LMÍ ($\sim 10 \times 10$ m) datasets using Esri flow routing algorithms. We used the ASTER GDEM drainage networks because in general they appear to have higher vertical resolution and greater planform fidelity than the LMÍ derived datasets. Extracted drainage patterns were compared to satellite imagery and our photogrammetry DEM to ensure fidelity. A minimum drainage accumulation area of 2.5×10^7 m^2 was used. River stretches located above and beneath ice caps were excluded from the dataset. We inverted our drainage inventory of 533 rivers across Iceland extracted from the ASTER GDEM to calculate uplift rate histories (Rudge et al., 2015). To do so we solved a version stream power model, which calculates rate of change of elevation, $\partial z/\partial t$, such that

$$\frac{\partial z}{\partial t} = -vA(x)^m \frac{\partial z}{\partial x} + U(x,t), \tag{11}$$

where U is uplift rate, which can vary as a function of space, x and time, t. A is upstream drainage area, which can be measured from a digital elevation model (Rosenbloom and Anderson, 1994; Rudge et al., 2015). v and m are positive constants that must be calibrated. From retreat rates in Fig. 7, we use $v = 8.3$ Ma^{-1} (see previous section for derivation). To invert for a spatio-temporal uplift history we use a damped least squares approach to minimize

$$|M\mathbf{U} - \mathbf{z}|^2 + \lambda_S^2 |S\mathbf{U}| + \lambda_T^2 |T\mathbf{U}|^2 \quad \text{subject to} \quad \mathbf{U} \geq 0, \tag{12}$$

where λ_S and λ_T control spatial and temporal smoothing of the model, respectively (Rudge et al., 2015). We ran multiple joint-inversions, which suggest that, for both ASTER and LMÍ derived data, best fitting $m = 0.5$. The best-fitting value of m was obtained from a systematic sweep of $0 \leq m \leq 1$ and setting $\lambda_S = 1$ and $\lambda_T = 0$. We acknowledge that m and λ_s trade-off to some extent. Drainage planforms are assumed to be stationary during the model runtime (Holocene), which is probably appropriate since all major rivers flow along deep valleys established before 10 ka. Model fits to rivers are good (residual rms misfit = 1.30 for data variance of 20 m; Figs. 9a–d) and results for cumulative uplift for the last 9 ka are shown in Fig. 9e.

8. Discussion

Calculated Holocene cumulative uplift and uplift rates are greatest in central Iceland where they exceed 100 m and 10 mm a^{-1}, respectively (Fig. 9e). Our calculated uplift exceeds 50 m in the Eastern and Western Volcanic zones, which are situated above Iceland's rift systems. Independent biostratigraphic and geophysical observations can be used to test the calculated uplift history and examine sources of Holocene uplift. Mapping of paleo-coastlines around Iceland indicate uplift rates of 0–15 mm a^{-1} during the last 8 ka (Le Breton et al., 2010). Average calculated cumulative uplift at these locations is 13 m, which yields an average Holocene-Recent coastal uplift of 13 mm a^{-1}. Preboreal aged marine mollusc and barnacle shells crop out at elevations of up to 40 m in southern Iceland (e.g. Berufjörður fjord), which suggests average uplift rates during the last 10 ka of 7 ± 2 mm a^{-1} (Nordhdahl and Pétursson, 2005). Calculated uplift rates in this region are 6.8 mm a^{-1}. The Plio-Pleistocene Tjörnes Beds Formations in North Iceland contain 1200 m thick sequences of shallow marine sediments and terrestrial deposits alternated with lava flows, which suggest that Iceland has been uplift by hundreds of meters since $\sim$5 Ma (see Fig. 1f; Verhoeven et al., 2011). Calculated cumulative Holocene uplift from our model in this region is > 70 m.

The elevation of the highest terrace and the oldest ages in the canyon indicate that denudation of the Jökulsárglúfur was up to $\sim$100 m since deglaciation (Fig. 6c; topmost terrace = $\sim$315 m, river bottom = $\sim$210 m). Denudational unloading, D, and isostatic adjustment generates rock uplift, U_D. We calculate $U_D = D\rho_c/\rho_a \approx 0.9D$ for crustal and asthenospheric densities of $\rho_c = 2800$ kg m^{-3}, $\rho_a = 3200$ kg m^{-3}, respectively. Using these values yields up to 90 m of regional rock uplift from denudation of Jökulsárglúfur. Uplift rates are $\lesssim 9$ mm a^{-1}, assuming unloading rates remained constant for 10 ka. Viscoelastic models indicate that present-day glacial isostatic adjustment exceeds 20 mm a^{-1} close to Vatnajökull and is negligible $\sim$100 km away from the centre of the modern glacier (i.e. close to the canyon; Árnadóttir et al., 2009). These uplift rates suggest the broad area of uplift measured from GPS data in central and southeastern Iceland can be explained by ablation of Iceland's largest glaciers. However, applying corrections for glacial isostatic adjustments to GPS uplift data results in areas of significant residual uplift which cannot be explained by glacial rebound (Schmidt et al., 2012). The largest residual vertical velocities (7–9 mm a^{-1}) are centred on Jökulsárgljúfur and are consistent with our calculated rates due to denudational unloading of the canyon.

Away from the canyon and Vatnajökull, highest values of calculated cumulative uplift coincide with loci of active seismicity along Iceland's rift systems and youngest rocks (Fig. 9; Tryggvason, 1973). Finally, a long wavelength (island-wide) component of cumulative uplift with an amplitude of a few tens of meters is required to fit observed longitudinal river profiles, which may be a manifestation of dynamic support generated by the Icelandic plume.

9. Conclusions

^{3}He dating and UAV photogrammetry of fluvial terraces constrain the history of one of Iceland's largest canyons, suggesting that knickpoint propagation occurred progressively during the Holocene. The canyon sits within one of the broad knickzones that are observed on all large Icelandic rivers. Measured retreat rates indicate the Jökulsárgljúfur knickpoint has been propagating at a rate of $\sim$0.7 m a^{-1} upstream during the last 8 ka, contrary to previous models which suggest discrete outburst floods as the dominant mode of canyon erosion. These retreat rates are consistent with simple block toppling calculations using present-day discharge which suggest toppling retreat rates range between $\sim$0.1–1 m a^{-1} and are strongly correlated to column height. A calibrated erosional model is used to invert drainage networks for a spatio-temporal history of Holocene uplift, which yields results that are broadly consistent with independent spot measurements. Calculated uplift patterns are highest near the centre of the island, close to the Vatnajökull glacier, and along the volcanic zones.

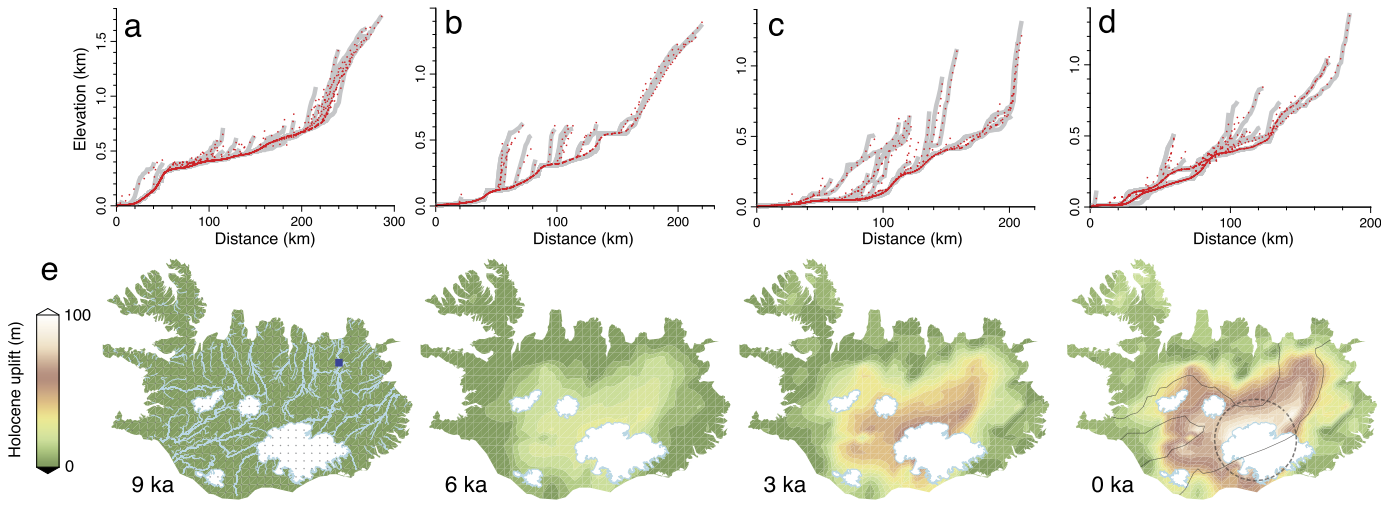

Fig. 9. Holocene uplift of Iceland. (a) Grey lines = longitudinal river profiles measured from Jökullsá á Fjöllum catchment; red dotted lines = best-fitting theoretical river profiles calculated from uplift history shown in panel (e). (a–d) Observed and best-fitting theoretical river profiles from Jökulsá á Brú, Ölfusá and Skálfandafljót catchments. Global residual rms misfit = 1.30. (e) Colour scale = calculated cumulative uplift from 9 ka to present-day; black dots = nodes in uplift model which are spaced 12.5 km apart; blue lines = 553 rivers used in inversion, blue square = location of Jökulsárgljúfur. Solid black lines encloses youngest (<0.7 Ma) rocks and rift zones (Jóhannesson and Sæmundsson, 1989); dashed black circle = location of plume centre (Shorttle et al., 2010); white polygons = modern glaciers.

These results indicate that a combination of rifting, post-glacial rebound, and sub-plate support generated tens of meters of uplift and erosion of Iceland's landscape during the last ∼9 ka. Our results suggest that progressive fluvial erosion plays an important role in generating relief in previously glaciated and volcanic landscapes on timescales of a few thousand years.

Data statement

Correspondence, material, data, and code requests should be addressed to g.stucky-de-quay14@imperial.ac.uk or gareth.roberts@imperial.ac.uk.

Acknowledgements

G.S.Q. was supported by a NERC PhD scholarship. We thank the Royal Society for financial support (Grant RG160020). K. Farley, J. Treffkorn, and M. Lamb are thanked for access to the Noble Gas Laboratory at Caltech and for helpful discussion. We thank P. Mason, J. Weddepohl, and A. Leggett for field and laboratory assistance. We thank two anonymous reviewers for their careful reading of our manuscript and their many insightful comments and suggestions. We are grateful to the Vatnajökull National Park and the Icelandic Institute for Natural History for permission to sample, export rocks, and fly drones.

References

Alho, P., Russell, A.J., Carrivick, J.L., Käyhkö, J., 2005. Reconstruction of the largest Holocene jökulhlaup within Jökulsá á Fjöllum, NE Iceland. Quat. Sci. Rev. 24 (22), 2319–2334.

Árnadóttir, T., Lund, B., Jiang, W., Geirsson, H., Björnsson, H., Einarsson, P., Sigurdsson, T., 2009. Glacial rebound and plate spreading: results from the first countrywide GPS observations in Iceland. Geophys. J. Int. 177 (2), 691–716.

Batchelor, G., 1967. An Introduction to Fluid. Dynamics. Cambridge University.

Baynes, E.R., Attal, M., Dugmore, A.J., Kirstein, L.A., Whaler, K.A., 2015a. Catastrophic impact of extreme flood events on the morphology and evolution of the lower Jökulsá á Fjöllum (northeast Iceland) during the Holocene. Geomorphology 250, 422–436.

Baynes, E.R., Attal, M., Niedermann, S., Kirstein, L.A., Dugmore, A.J., Naylor, M., 2015b. Erosion during extreme flood events dominates Holocene canyon evolution in northeast Iceland. Proc. Natl. Acad. Sci. 112 (8), 2355–2360.

Baynes, E.R., Lague, D., Attal, M., Gangloff, A., Kirstein, L.A., Dugmore, A.J., 2018. River self-organisation inhibits discharge control on waterfall migration. Sci. Rep. 8 (1), 2444.

Björnsson, H., 1980. Avalanche activity in Iceland, climatic conditions, and terrain features. J. Glaciol. 26 (94), 9–12.

Bjornsson, H., 2009. Jokulhlaups in Iceland: Sources, Release, and Drainage. Megaflooding on Earth and Mars. Cambridge University Press, Cambridge, pp. 50–64.

Blard, P.-H., Balco, G., Burnard, P., Farley, K., Fenton, C., Friedrich, R., Jull, A.T., Niedermann, S., Pik, R., Schaefer, J., et al., 2015. An inter-laboratory comparison of cosmogenic ^{3}He and radiogenic ^{4}He in the CRONUS-P pyroxene standard. Quat. Geochronol. 26, 11–19.

Crochet, P., Jóhannesson, T., Jónsson, T., Sigurdsson, O., Björnsson, H., Pálsson, F., Barstad, I., 2007. Estimating the spatial distribution of precipitation in Iceland using a linear model of orographic precipitation. J. Hydrometeorol. 8 (6), 1285–1306.

Dunai, T.J., 2000. Scaling factors for production rates of in situ produced cosmogenic nuclides: a critical reevaluation. Earth Planet. Sci. Lett. 176 (1), 157–169.

Dunne, J., Elmore, D., Muzikar, P., 1999. Scaling factors for the rates of production of cosmogenic nuclides for geometric shielding and attenuation at depth on sloped surfaces. Geomorphology 27 (1–2), 3–11.

Einarsson, M.Á., 1984. Climate of Iceland, 000072851.

Elíasson, S., 1974. Eldsumbrot í Jökulsárgljúfrum. Jökull 44.

Eythorsson, J., Sigtryggsson, H., Bertelsen, E., 1971. Pt. 3: The Climate and Weather of Iceland. Munksgaard.

Fenton, C.R., Niedermann, S., Goethals, M.M., Schneider, B., Wijbrans, J., 2009. Evaluation of cosmogenic ^{3}He and ^{21}Ne production rates in olivine and pyroxene from two Pleistocene basalt flows, western Grand Canyon, AZ, USA. Quat. Geochronol. 4 (6), 475–492.

Geirsdóttir, Á., Miller, G.H., Andrews, J.T., 2007. Glaciation, erosion, and landscape evolution of Iceland. J. Geodyn. 43 (1), 170–186.

Gosse, J.C., Phillips, F.M., 2001. Terrestrial in situ cosmogenic nuclides: theory and application. Quat. Sci. Rev. 20 (14), 1475–1560.

Henriksen, S., 2005. Travel Time for Flow in Jökulsá á Fjöllum in Relation to Discharge and Sediment Transport. Orkustofnun (National Energy Authority).

Jóhannesson, H., Sæmundsson, K., 1989. Geological Map of Iceland (1:500 000), Bedrock Geology, 1st edn.

Jones, S.M., White, N., Maclennan, J., 2002. V-shaped ridges around Iceland: implications for spatial and temporal patterns of mantle convection. Geochem. Geophys. Geosyst. 3 (10), 1–23.

Jónsdóttir, J.F., Uvo, C.B., 2009. Long-term variability in precipitation and streamflow in Iceland and relations to atmospheric circulation. Int. J. Climatol. 29 (10), 1369–1380.

Kjær, K.H., Korsgaard, N.J., Schomacker, A., 2008. Impact of multiple glacier surges: a geomorphological map from Brúarjökull, East Iceland. J. Maps 4 (1), 5–20.

Koppes, M.N., Montgomery, D.R., 2009. The relative efficacy of fluvial and glacial erosion over modern to orogenic timescales. Nat. Geosci. 2 (9), 644.

Lal, D., 1991. Cosmic ray labeling of erosion surfaces: in situ nuclide production rates and erosion models. Earth Planet. Sci. Lett. 104 (2–4), 424–439.

Lamb, M.P., Dietrich, W.E., 2009. The persistence of waterfalls in fractured rock. Geol. Soc. Am. Bull. 121 (7–8), 1123–1134.

Le Breton, E., Dauteuil, O., Biessy, G., 2010. Post-glacial rebound of Iceland during the Holocene. J. Geol. Soc. 167 (2), 417–432.

Licciardi, J., Kurz, M., Curtice, J., 2006. Cosmogenic ^{3}He production rates from Holocene lava flows in Iceland. Earth Planet. Sci. Lett. 246 (3), 251–264.

Lifton, N.A., Bieber, J.W., Clem, J.M., Duldig, M.L., Evenson, P., Humble, J.E., Pyle, R., 2005. Addressing solar modulation and long-term uncertainties in scaling secondary cosmic rays for in situ cosmogenic nuclide applications. Earth Planet. Sci. Lett. 239 (1–2), 140–161.

Marrero, S.M., Phillips, F.M., Borchers, B., Lifton, N., Aumer, R., Balco, G., 2016. Cosmogenic nuclide systematics and the CRONUScalc program. Quat. Geochronol. 31, 160–187.

Martin, E., Paquette, J.-L., Bosse, V., Ruffet, G., Tiepolo, M., Sigmarsson, O., 2011. Geodynamics of rift–plume interaction in Iceland as constrained by new $^{40}Ar/^{39}Ar$ and in situ U–Pb zircon ages. Earth Planet. Sci. Lett. 311 (1–2), 28–38.

Nordhdahl, H., Ingólfsson, Ó., Pétursson, H.G., Hallsdóttir, M., 2008. Late Weichselian and Holocene environmental history of Iceland. Jökull 58, 343–364.

Nordhdahl, H., Pétursson, H.G., 2005. 3. Relative sea-level changes in Iceland: new aspects of the Weichselian deglaciation of Iceland. In: Developments in Quaternary Sciences. Elsevier, pp. 25–78.

Ólafsson, H., Furger, M., Brummer, B., 2007. The weather and climate of Iceland. Meteorol. Z. 16 (1), 5–8.

Pagli, C., Sigmundsson, F., Lund, B., Sturkell, E., Geirsson, H., Einarsson, P., Árnadóttir, T., Hreinsdóttir, S., 2007. Glacio-isostatic deformation around the Vatnajökull ice cap, Iceland, induced by recent climate warming: GPS observations and finite element modeling. J. Geophys. Res., Solid Earth 112. B8.

Parnell-Turner, R., White, N., Henstock, T., Murton, B., Maclennan, J., Jones, S.M., 2014. A continuous 55-million-year record of transient mantle plume activity beneath Iceland. Nat. Geosci. 7 (12), 914.

Protin, M., Blard, P.-H., Marrocchi, Y., Mathon, F., 2016. Irreversible adsorption of atmospheric helium on olivine: a lobster pot analogy. Geochim. Cosmochim. Acta 179, 76–88.

Rosenbloom, N.A., Anderson, R.S., 1994. Hillslope and channel evolution in a marine terraced landscape, Santa Cruz, California. J. Geophys. Res., Solid Earth 99 (B7), 14013–14029.

Rudge, J.F., Roberts, G.G., White, N.J., Richardson, C.N., 2015. Uplift histories of Africa and Australia from linear inverse modeling of drainage inventories. J. Geophys. Res., Earth Surf. 120 (5), 894–914.

Sato, T., Niita, K., 2006. Analytical functions to predict cosmic-ray neutron spectra in the atmosphere. Radiat. Res. 166 (3), 544–555.

Schmidt, P., Lund, B., Arnadottir, T., Schmeling, H., 2012. Glacial isostatic adjustment constrains dehydration stiffening beneath Iceland. Earth Planet. Sci. Lett. 359, 152–161.

Shorttle, O., Maclennan, J., Jones, S., 2010. Control of the symmetry of plume-ridge interaction by spreading ridge geometry. Geochem. Geophys. Geosyst. 11 (7).

Smith, L.C., Alsdorf, D.E., Magilligan, F.J., Gomez, B., Mertes, L.A., Smith, N.D., Garvin, J.B., 2000. Estimation of erosion, deposition, and net volumetric change caused by the 1996 Skeidharársandur jökulhlaup, Iceland, from synthetic aperture radar interferometry. Water Resour. Res. 36 (6), 1583–1594.

Spedding, N., Evans, D.J., 2002. Sediments and landforms at Kvíárjökull, southeast Iceland: a reappraisal of the glaciated valley landsystem. Sediment. Geol. 149 (1–3), 21–42.

Stone, J.O., 2000. Air pressure and cosmogenic isotope production. J. Geophys. Res., Solid Earth 105 (B10), 23753–23759.

Sturkell, E., Einarsson, P., Sigmundsson, F., Geirsson, H., Olafsson, H., Pedersen, R., de Zeeuw-van Dalfsen, E., Linde, A.T., Sacks, S.I., Stefánsson, R., 2006. Volcano geodesy and magma dynamics in Iceland. J. Volcanol. Geotherm. Res. 150 (1–3), 14–34.

Tentler, T., Temperley, S., 2007. Magmatic fissures and their systems in Iceland: a tectonomagmatic model. Tectonics 26 (5).

Tryggvason, E., 1973. Seismicity, earthquake swarms, and plate boundaries in the Iceland region. Bull. Seismol. Soc. Am. 63 (4), 1327–1348.

Verhoeven, K., Louwye, S., Eiríksson, J., De Schepper, S., 2011. A new age model for the Pliocene–Pleistocene Tjörnes section on Iceland: its implication for the timing of North Atlantic–Pacific palaeoceanographic pathways. Palaeogeogr. Palaeoclimatol. Palaeoecol. 309 (1–2), 33–52.

Waitt, R., 2009. Great Holocene floods along Jökulsá á Fjöllum, north Iceland. Flood and megaflood processes and deposits: recent and ancient examples. Spec. Publ. Int. Assoc. Sedimentol. 32, 37–51.

Whipple, K.X., Tucker, G.E., 1999. Dynamics of the stream-power river incision model: implications for height limits of mountain ranges, landscape response timescales, and research needs. J. Geophys. Res., Solid Earth 104 (B8), 17661–17674.